M-shaped specimen for the high strain rate tensile testing using a Split Hopkinson bar apparatus

Dirk Mohr, Gérard Gary

M-shaped Specimen for the High-strain Rate Tensile Testing Using a Split Hopkinson Pressure Bar Apparatus

D. Mohr · G. Gary

Abstract An experimental technique is proposed to determine the tensile stress–strain curve of metals at high strain rates. An M-shaped specimen is designed which transforms a compressive loading at its boundaries into tensile loading of its gage section. The specimen can be used in a conventional split Hopkinson pressure bar apparatus, thereby circumventing experimental problems associated with the gripping of tensile specimens under dynamic loading. The M-specimen geometry provides plane strain conditions within its gage section. This feature retards necking and allows for very short gage sections. This new technique is validated both experimentally and numerically for true equivalent plastic strain rates of up to 4,250/s.

Keywords Finite element analysis · Fracture · High strain rates · Hopkinson bar · Kolsky bar · Plasticity · Tensile testing · Transverse plane strain

Introduction

The virtual design of engineering structures subject to impact loading requires reliable experimental data for the development and calibration of computational material models. It is common practice to make use of the split Hopkinson pressure bar (SHPB) technique [1, 2] to determine the dynamic response of materials under uniaxial compressive loading. In addition to compression testing, the split Hopkinson bar technique has been developed for the torsion testing of hollow cylindrical specimens [3]. Direct dynamic tensile tests may also be performed by the means of the split Hopkinson bar apparatus [4]. However, due to experimental difficulties, direct dynamic tensile tests are not very often used to characterize the high strain rate response of engineering materials. Consequently, most existing strain-rate dependent plasticity models have been developed on the basis of experimental data for uniaxial compression and torsion.

While the deformation response of metals under tension at high strain rates may be estimated within reasonable accuracy based on data for compression or shear, dynamic tensile tests are indispensable in characterizing the crack initiation in metals. Most challenges in designing dynamic tensile experiments are related to the gripping of the specimen. When measuring the forces and displacements by means of bars, the tensile specimen needs to be attached to the respective ends of the so-called incident and transmitter bars. For this, specimens with threaded specimen shoulders are usually directly screwed into the bar ends. As pointed out by Nicholas [5], reliable testing of threaded specimens requires the elimination of all play from the joints; in addition, perfect alignment of short tensile specimens is needed [4]. The threads inside the bar ends cause spurious wave reflections in the vicinity of the bar-specimen interface. Failure to eliminate all gaps amplifies these reflections further, making it difficult to obtain

D. Mohr · G. Gary
Solid Mechanics Laboratory, CNRS UMR 7649,
Department of Mechanics, École Polytechnique,
91128 Palaiseau Cedex, France

D. Mohr (✉)
Impact and Crashworthiness Laboratory, Department of Mechanical Engineering, Massachusetts Institute of Technology,
Cambridge, MA, USA
e-mail: mohr@mit.edu

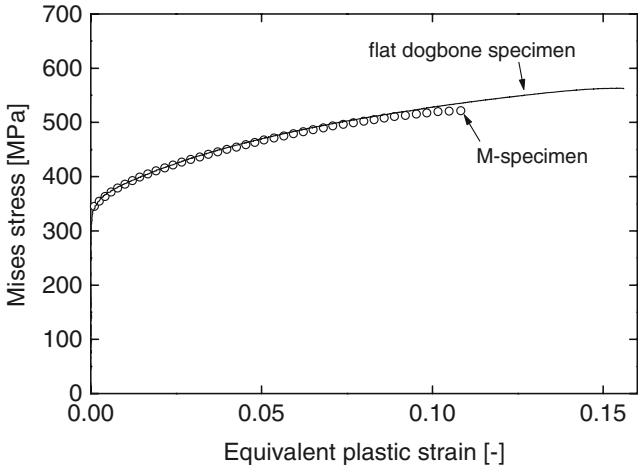

Fig. 1 Stress-strain curve of aluminum 2024-T351 (von Mises stress versus equivalent plastic strain). The solid line shows the result of a uniaxial tensile test on a flat dogbone specimen (measured outside the neck). The open dots depict the stress-stain curve determined from the quasi-static testing of the M-specimen

accurate measurements of the forces and displacements at the specimen boundaries.

In this paper, we propose a specimen for tensile testing in a split Hopkinson pressure bar apparatus. In close conceptual analogy with Luong's tensile specimen for geological materials [6], the specimen transforms an incident pressure pulse at its boundaries into tensile loading of its gage section. The key advantage of this technique is that these tests may be performed without attaching the specimen to the bar ends. Instead, the specimen is freely positioned between the flat ends of the incident and transmitter bars. Moreover, a conventional split Hopkinson pressure bar apparatus may be used to generate the loading, thereby avoiding several difficulties related to the generation of a tensile pulse in the incident bar.

Materials and Methods

All specimens are made from aluminum 2024-T351. The reference stress–strain curve for static loading (2 mm/min) is determined from uniaxial tensile tests on flat dogbone-shaped specimens of 3.5 mm thickness (gage section dimensions: 8.95 mm wide and 57.15 mm long). The solid curve in Fig. 1 shows the true stress as a function of the logarithmic plastic strain. A Young's modulus of E= 73,980 MPa is found from optical displacement measurements (digital image correlation). The material begins to deform plastically at a true stress of about s_0=330 MPa and exhibits strain hardening up to about 550 MPa. In the uniaxial test, necking initiates at a plastic strain of about 0.15. The mass density of Al2024-T351 is ρ=2.8 g/cm^3 which corresponds to a uniaxial wave propagation speed of about $c_0 = \sqrt{E/\rho} = 5,140\,\mathrm{m/s}$.

M-shaped Specimen

Design Concept

Figure 2(a) shows the front view of the proposed specimen. It is called 'M-specimen' because its shape resembles the letter 'M.' The M-specimen is designed to transform a compressive loading at its boundaries into tensile loading of its two gage sections. In the following, we discuss the specimen geometry by considering the specimen as a series of beam segments of length l_i and of cross-sectional height h_i. Dashed lines in Fig. 2(a) represent the corresponding beam segment mid-axes. As illustrated by the free body diagram [Fig. 2(b)], the segment between the points E and F is predominantly under compression. Similarly, the segment A–B is subject to compressive loading while the segments B–C and D–E are subject to shear and bending

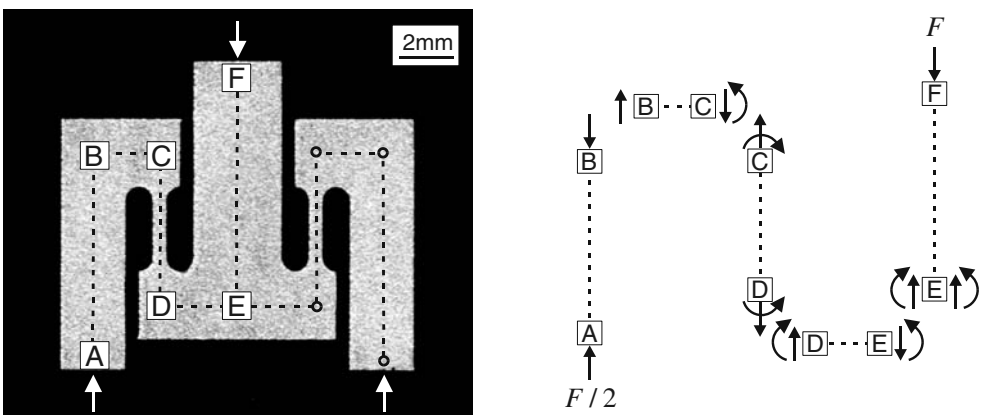

Fig. 2 (**a**) Photograph of the EDM machined specimen, (**b**) simplified free-body diagram depicting the generalized forces acting on individual sections of the specimen

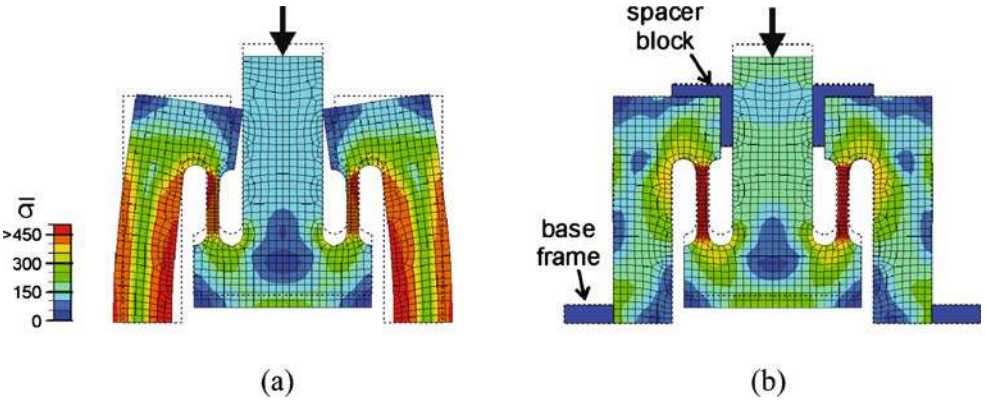

Fig. 3 Finite element estimation of the M-specimen response after applying a vertical displacement of 0.5 mm under static conditions: (**a**) without and (**b**) with spacer blocks and base frame. The dashed lines indicate the initial shape of the specimen (identical for both configurations); the superposed contour plot shows the von Mises stress distribution within the specimen

loading. The specimen gage sections (segment C–D) are predominantly stretched. The key considerations in choosing the specimen dimensions are:

(1) Limit plastic deformation to the gage section. The dimensions of the specimen must be chosen such that the gage section deforms plastically while the remaining specimen structure responds in a purely elastic manner.

(2) Minimize bending deformation. The bending of the sections D–E and B–C affects the stress and strain uniformity within the specimen gage section (observe from Fig. 2(b) that there is a constant bending moment $M = 0.5Fl_{B-C}$ acting on segment D–C). In addition, the bending-induced rotation of point D may disturb the otherwise uniform fields within the gage section [Fig. 3(a)]. To minimize the bending effects, the length of the segments B–C and D–E should be as small as possible. This can be achieved by reducing the heights h_{F-E} and h_{A-B}, the corner radii, the width of the vertical slots, and the gage section thickness a. Furthermore, increasing the height h_{D-E} of section D–E reduces the bending-induced rotation of point D.

(3) Prevent buckling of the segment A–B. The slender segment A–B is subject to compressive loading and therefore prone to buckling. The minimal length l_{A-B} is determined by the length of the gage section, the height of the bent-sections D–E and B–C, and the displacement to fracture of the gage sections. Observe that the spacing between the specimen and the bottom loading platen of the testing machine (just below point E) needs to be sufficiently large to avoid contact prior to specimen fracture. Increasing the cross-sectional height of the section A–B would be beneficial, but this measure would also reduce the advantageous wave guidance by this particular section.

(4) Minimize the distance of wave travel. The maximum acceptable loading velocity is limited by the time it takes for an incoming stress wave to travel from the top to the bottom boundary of the specimen. This characteristic duration of wave travel must be short as compared to the duration of significant changes in the force level in order to guarantee quasi-static equilibrium throughout dynamic testing. Consequently, the total distance of wave travel along the path F-E-D-C-B-A shall be short. Note that this distance depends on the maximum force within the gage section and on the gage section length. The higher the maximum force, the larger the required dimensions of the 'support structure' around the gage section (e.g. the height of sections B–C or D–E). Furthermore, the longer the gage section, the longer of sections A–B and E–F. Therefore, it is desirable to keep both the gage thickness and length small. Keeping the gage length small also increases the maximum strain rate at which the specimen is still in quasi-static equilibrium.

(5) Achieve transverse plane strain conditions. The stress and strain fields also depend on the specimen width i.e. the dimension perpendicular to the plane shown in Fig. 2(a). If the specimen width w is of the order of the gage section thickness, the stress state within the gage section is uniaxial. However, in view of problems related to the specimen alignment (with respect to the loading platens) as well as the onset of fracture near the corner radii, the specimen width must be large as compared to the gage section thickness a and gage length l,

$$w \gg a \text{ and } w \gg l$$

which ultimately guarantees transverse plane strain conditions within the gage section. In other words, the strains along the width direction are approximately zero, $\varepsilon_{zz} \cong 0$. Detailed analysis of transverse plane strain specimens [7] has shown that the stress and strain fields are perturbed along a characteristic distance from the free boundary. One can either correct for such perturbations using simplified formulas or chose w sufficiently large such that these perturbations may be neglected.

Based on the above considerations, we conclude that the gage section should be as thin and short as possible for optimal specimen performance in terms of field uniformity within the gage section and of maximum strain rate. Here, we chose a gage section thickness of a=0.5 mm which results in overall specimen dimensions that can still be manufactured within reasonable accuracy using a computer-controlled wire EDM [Fig. 2(a)]. We use a set of spacer blocks [see Fig. 3(b)] to prevent the bending-induced lateral motion of point C. In addition, an exterior base frame is put in place to prohibit the lateral motion of point A. As a result, the effective buckling length of section A–B is significantly increased, thereby improving the specimen's structural stability and stress uniformity within the gage sections.

Determination of the Stress–strain Curve

Throughout the experiment, the forces and displacements are measured at the specimen boundaries, i.e. at the top and bottom surfaces of the M-specimen. Assuming that the specimen is in quasi-static equilibrium (F_{top}=F_{bot}), the resulting experimental output is a single force–displacement curve $F(u)$ where $u = u_{top} - u_{bot}$. In the following, we determine the stress–strain curve from experiments on specimens made of Levy–von Mises materials. For small to moderate deformations, it is assumed that the total displacement corresponds to the sum of the elastic part, u_e, which is proportional to the actual applied force, and the plastic part, u_p, which results from the plastic deformation of the specimen gage sections,

$$u = u_e + u_p \tag{1}$$

and

$$F = Ku_e \tag{2}$$

where the stiffness K accounts for the elastic stiffness of the specimen (including the gage section) and of the testing device. The nominal stress along the gage length, $\sum_{yy}$, reads

$$\sum\nolimits_{yy}(t) = \frac{F(t)}{A_0} \tag{3}$$

where A_0= $2aw$ denotes the total initial cross-sectional area of the gage sections. Assuming a constant effective gage section length l_{eff} [Fig. 7(b)], the corresponding nominal plastic strain, E^p_{yy}, reads:

$$E^p_{yy}(t) = \frac{u_p}{l_{\text{eff}}} = \frac{u(t)}{l_{\text{eff}}} - \frac{F(t)}{Kl_{\text{eff}}} \tag{4}$$

Assuming purely deviatoric plasticity (zero volumetric strain), we calculate the true stress

$$\sigma_{yy} = \left(1 + E^p_{yy}\right)\Sigma_{yy}. \tag{5}$$

The logarithmic (true) plastic strain is:

$$\varepsilon^p_{yy} = \ln\left(1 + E^p_{yy}\right) \tag{6}$$

Assuming transverse plane strain conditions (along with the von Mises yield surface), we have the corresponding equivalent plastic strain:

$$\overline{\varepsilon}^p(t) = \frac{2}{\sqrt{3}}\varepsilon^p_{yy}(t) \tag{7}$$

and the equivalent von Mises stress

$$\overline{\sigma}(t) = \frac{\sqrt{3}}{2}\sigma_{yy}(t) \tag{8}$$

Thus, using equations (7) and (8), the stress–strain curve $\overline{\sigma} = \overline{\sigma}(\overline{\varepsilon}^p)$ can be determined based on the experimental measurements $F(t)$ and $u(t)$ (provided that K is identified with the initially purely elastic response of the specimen).

Effect of the Specimen Width

The procedure of determining the stress–strain curve from the measured force and displacement histories at the specimen boundaries requires that the assumption of transverse plane strain holds true within the specimen cross-section. In a computational model, we may directly impose plane strain conditions to obtain a reference solution. Subsequently, fully three-dimensional computational models are used to demonstrate the effect of the finite specimen width on the experimental results. It is noted that the effect of specimen width in the case of the M-specimen is conceptually very similar to conventional flat transverse plane strain specimens.

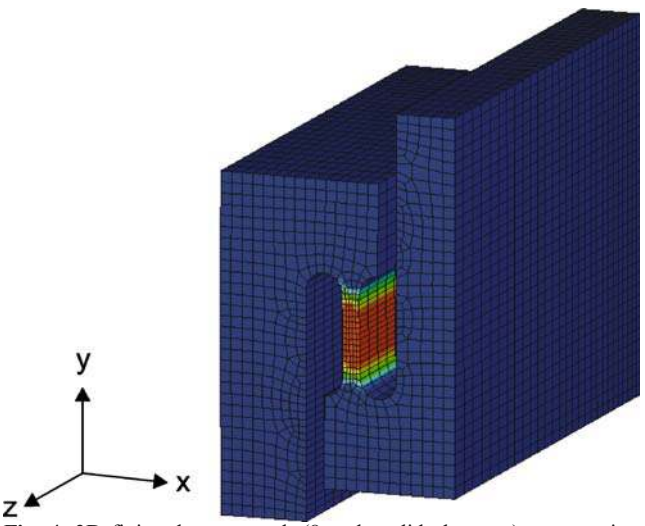

Fig. 4 3D finite element mesh (8-node solid elements) representing one quarter of the w=28 mm wide M-specimen (symmetry planes x–y and y–z); the contour plot indicates the intensity of the equivalent plastic strain

Figure 4 shows a three-dimensional finite element discretization of the M-specimen using 8-node reduced-integration solid elements. The model makes use of the specimen and loading symmetry with respect to both the x–y and y–z-planes. Simulations are performed for w=14 mm, 28 mm and 56 mm (Abaqus/implicit, geometrically nonlinear static analysis, J2-plasticity model calibrated against the uniaxial tensile test data for Al2024-T351). In addition, a simulation with perfect plane strain conditions is carried out by setting the z-displacement of all nodes equal to zero. Figure 5(b) summarizes the computed force (per unit width) versus vertical displacement. It shows that the force level is a function of the specimen width. The wider the specimen, the closer the force-displacement history follows the upper curve for perfect plane strain conditions. The lower force level for specimens of finite width is due to the free boundary effect at the maximum and minimum z-coordinate where $\varepsilon_{zz}=0$ and $\sigma_{zz}=0$. The resulting axial load carrying capacity of the Levy–von Mises material (effect of superposed hydrostatic tension) is lower near the boundary than near the specimen center ($\varepsilon_{zz} \cong 0$ and $\sigma_{zz} > 0$). A plot of the vertical stress σ_{yy} along the z-direction reveals that this perturbation is limited to a band of about 8 mm width, irrespectively of the overall specimen width [Fig. 5(a)]. Consequently, the effect of specimen width on the force level decreases monotonically for $w \to \infty$ [Fig. 5(b)]. In the present study, we chose a specimen width of about 30 mm. Thus, this specimen still fits on the flat ends of a 40 mm diameter Hopkinson pressure bar while the expected resultant error in the force level is less than 3%.

Validation for Static Loading

Computational Validation

The static finite element simulations of the M-specimen are also used to validate the above procedure of determining the stress–strain curve. When analyzing the numerical results, the macroscopically determined stress–strain curve may be directly compared with the material model input data used. Therefore, the use of numerical simulations provides a powerful means to study the validity of the proposed experimental technique.

Using the quarter model of the 28 mm wide M-specimen (Fig. 4), the force–displacement curve is computed up to a total displacement of 0.25 mm (in 25 implicit time steps). Subsequently, the evolutions of the plastic displacement $u_p(t)$ and of the von Mises stress $\overline{\sigma}(t)$ within the specimen gage section are calculated using the procedure outlined in the section "Determination of the Stress–strain Curve". The resultant stress–displacement curve corresponding to the 'global' measurement $F(t)$ is plotted in Fig. 6(a). The same figure also shows a dashed curve which depicts the evolution of the 'local' von Mises stress at the integration point of an 8-node reduced-integration solid element positioned near the gage section center. The comparison shows the excellent agreement of the local and global measurements of the von Mises stress. The relative deviation of about 3% is attributed to the finite width of the specimen. Due to the apparent proportionality of this error, one may correct for the effect of finite width by increasing the macroscopically determined curve by 3%.

Figure 6(b) shows the evolution of the equivalent plastic strain. It is found by matching the slopes of the locally and globally measured evolution curves that the length of the straight section (excluding transition radii) provides a good approximation for the effective gage length [Fig. 7(b)]. The

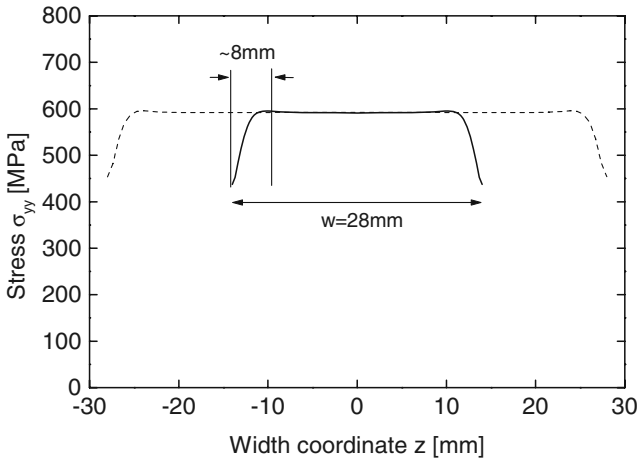

(a)

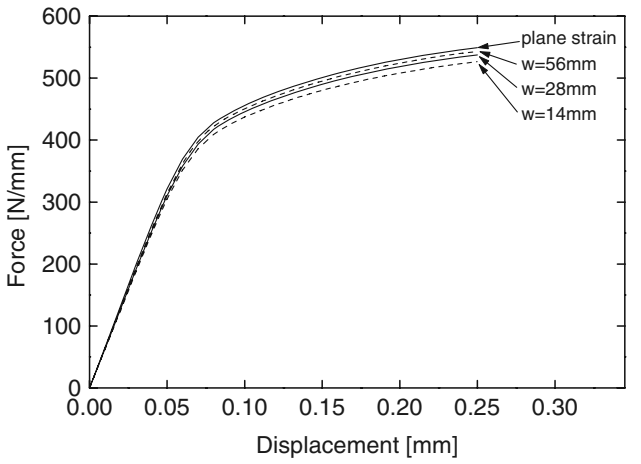

(b)

Fig. 5 FEA simulation results: (**a**) Vertical stress fields within the gage sections of specimens of width w=28 mm (*solid line*) and w=56 mm (*dashed line*); (**b**) force per unit width as a function of the applied displacement for specimens of different widths

curves follow each other very closely except for an initial offset in strain of about $\Delta\bar{\varepsilon}_p = 0.0025$. Note that according to equation (4) it is assumed that all nonlinearities in the global force–displacement curve are due to uniform plastic deformation within the gage section. However, the deflection of segments B–C and D–E involves the formation of plastic bending hinges at the points C and D before the gage section deforms plastically due to uniform stretching (Fig. 7). Once the initial yield stress has been overcome within the gage section, the plastic bending contribution to the overall plastic displacement becomes insignificant. As a result, we observe a constant offset between the local and global measurement of the equivalent plastic strain [Fig. 6(b)].

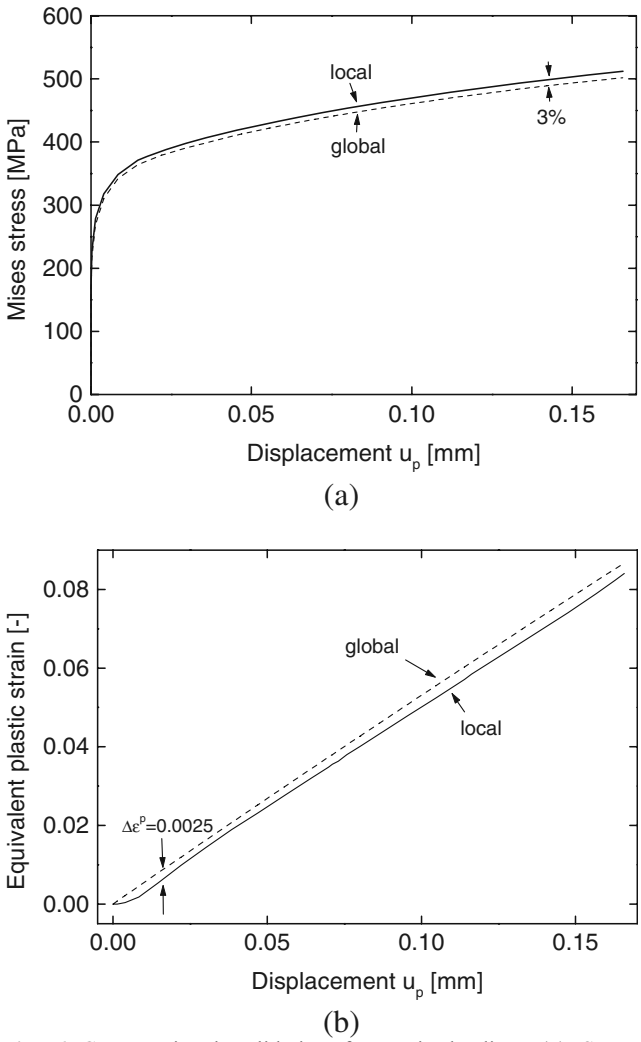

Fig. 6 Computational validation for static loading: (**a**) Stress evolution within the center of the gage section. The solid curve labeled 'exact FEA' depicts the stress evolution at the integration point of an 8-node element positioned within the central gage section while the dashed curve labeled 'analytical' is determined from the total force history at the specimen boundary. (**b**) Corresponding evolution of the equivalent plastic strain

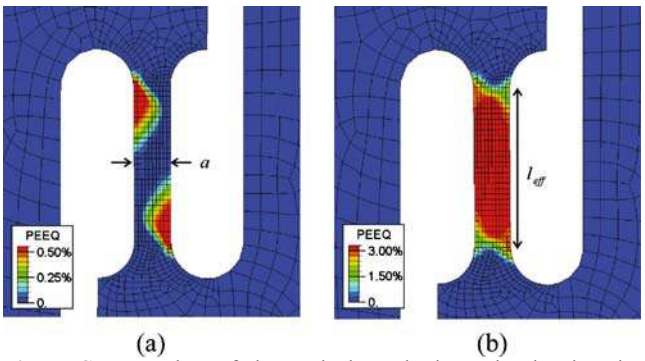

Fig. 7 Contour plots of the equivalent plastic strain showing the formation of plastic hinges prior to the 'uniform stretching' of the gage section: (**a**) μ_{pl}=0.004 mm, (**b**) μ_{pl}=0.05 mm. The results are obtained from a two-dimensional plane strain analysis (element type CPE4R in Abaqus/standard) including the spacer blocks

Experimental Validation

A specimen of 29.6 mm width is tested at a crosshead velocity of 5 mm/min using a screw-driven universal testing machine (Model G45, MTS, Eden-Prairie). The measured force–displacement curve $F(u)$ is depicted by the open dots in Fig. 8. The linear elastic part of this curve of slope K is due to elastic deformations of the loading device and of the specimen. The steeper solid curve represents the corresponding result as obtained from three-dimensional finite element simulations with infinite machine stiffness.

In order to compare the experiments and simulations, we calculated the plastic displacement according to equation (4) and plotted the resulting curves $F(u_p)$ in the same graph. Both curves (the left dashed and dotted curves in Fig. 8) are in excellent agreement, which confirms the reliability of the

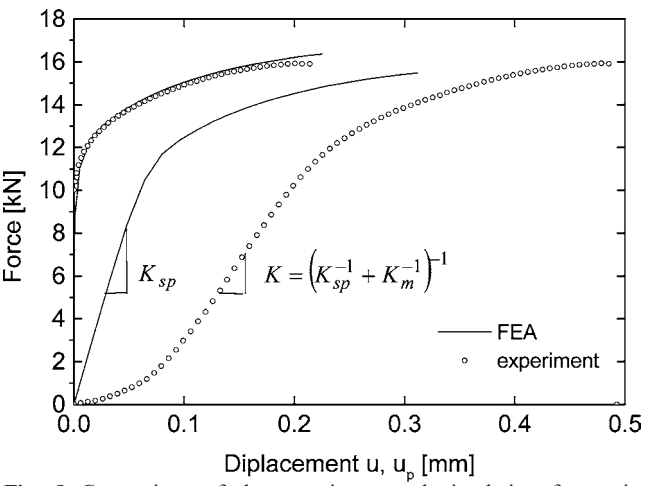

Fig. 8 Comparison of the experiment and simulation for static loading. The linear elastic part of the experimentally-measured force–displacement curve $F(u)$ corresponds to the sum of the machine stiffness K_m and the specimen stiffness K_{sp}. The two coinciding dotted and solid curves at the left depict the force as a function of the plastic displacement

static finite element model, notably the assumption of a Levy–von Mises material model for the Al2024-351. Since the procedure for determining the stress–strain curve has already been verified for the numerical model, it also holds true for the experimental measurements. The direct comparison of the results from experiments on the M-shaped specimen and flat tensile specimens (Fig. 1) demonstrates that both experimental techniques yield the same characteristic stress–strain curve for Al2024-T351 under static loading.

Validation for Dynamic Loading

The material characterization for dynamic loading requires the minimization of structural effects (lateral inertia) and of axial transient effects in the specimen. In particular, the specimen must be in quasi-static equilibrium throughout testing. In other words, the force–time histories at the top and bottom of the specimen must be approximately equal, i.e.

$$F_{\text{in}}(t) \cong F_{\text{out}}(t). \tag{9}$$

If this important condition of quasi-static equilibrium (which will be discussed in more detail below) is fulfilled, the above procedure for calculating the stress and strain histories within the M-specimen gage section can also be used in the dynamic case (provided that the Levy–von Mises assumptions will also hold true at high strain rates).

The path F-E-D-C-B-A is about $L \cong 30$ mm long and thus, the characteristic duration for a wave to travel through the entire specimen is about $L/C_0 \cong 5.7\mu s$. Recall from the static experiment that a total displacement of 0.5 mm induces an equivalent plastic strain of about 0.1. An estimated loading velocity of about 5 m/s would be required to attain this strain at a rate of 1,000/s. The duration of such an experiment would be about 100 μs which is still considerably long as compared to the characteristic duration of wave travel of 5.7 μs. Therefore, it may be expected that the specimen will still be in quasi-static equilibrium for strain rates of the order of 1,000/s. In the following, dynamic experiments are performed and analyzed in detail for average loading rates above 1,000/s. Numerical simulations are performed to gain further insight into the specimen response for high strain rates. Special attention will be paid to the fulfillment of the quasi-static equilibrium hypothesis for high loading velocities.

Split Hopkinson Pressure Bar Apparatus

A SHPB apparatus consisting of two aluminum bars and an aluminum striker bar is used to test the specimen under dynamic loading. All bars have a circular cross-section of 40 mm diameter. The lengths are 1,203 mm for the striker bar, 2,991 mm for the incident bar, and 1,850 mm for the transmitter bar. All contact surfaces at the bar ends are flat and perpendicular to the longitudinal bar axis. The mass density and longitudinal wave propagation speed of the bars are 2,820 kg/m^3 and 5,140 m/s, respectively. As shown in Fig. 9, the specimen is placed between the flat ends of the incident and transmitter bars. In the horizontal set-up, both the incident and transmitter bar are supported through translational bearings positioned at a spacing of about 500 mm. The impact velocity of the striker bar (average velocity prior to impact over 10 mm distance) is determined from optical measurements (high contrast grating of 1 mm pitch along with laser and photodiode). Strain gages positioned near the center of the incident bar (at a distance of 1,200 mm from the incident bar/specimen interface) and on the transmitter bar (at a distance of 335 mm from the transmitter bar/specimen interface) measure the strain history in the two bars. The amplified signal of the strain gages is recorded at a frequency of 1 MHz for the slow tests and 5 MHz for the fast tests. Figure 10 shows the characteristic incident wave trains as recorded by the incident strain gage after striker impact at v_{st}=4.1 m/s and v_{st}=9.4 m/s, respectively. The signal rises to its mean level within about 50 μs. Significant Pochhammer–Chree oscillations (of up to 10 kN magnitude) are observed for the highest loading velocity.

The experimental recordings are processed using the DAVID software package [8] following the procedures and requirements described in Zhao and Gary [9] and Gary [8].

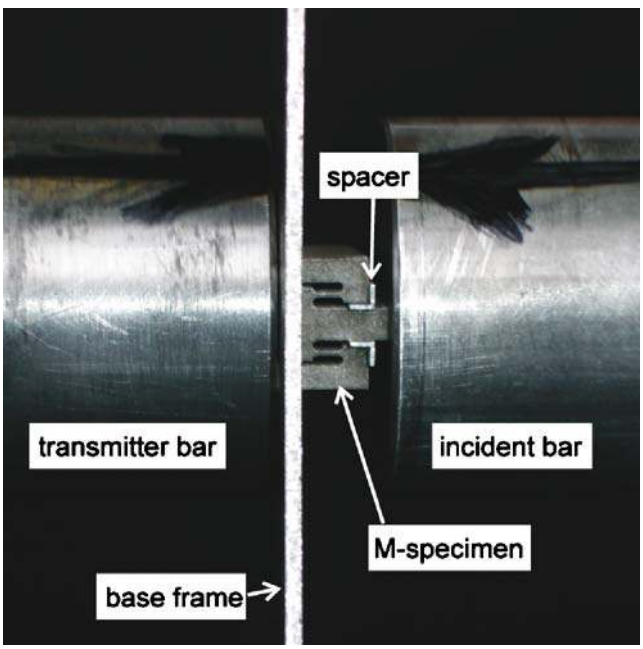

Fig. 9 Photograph of the M-specimen in the SHPB apparatus prior to testing

Accounting for geometric dispersion, the measured incoming and reflected waves are 'transported' to the specimen/incident bar interface, i.e. the top boundary of the specimen. Analogously, the measured transmitted wave is transported to the specimen/transmitter bar interface. Subsequently, the velocities and forces at the top and bottom specimen boundaries are calculated using the classical formulas

$$F_{\text{in}}(t) = E_{\text{bar}} A_{\text{bar}} [\varepsilon_{\text{in}}(t) + \varepsilon_{re}(t)] \tag{10}$$

$$F_{\text{out}}(t) = E_{\text{bar}} A_{\text{bar}} \varepsilon_{\text{bar}}(t) \tag{11}$$

and

$$v_{\text{in}}(t) = -C_{\text{bar}} [\varepsilon_{\text{in}}(t) - \varepsilon_{re}(t)] \tag{12}$$

$$v_{\text{out}}(t) = -C_{\text{bar}} \varepsilon_{tra}(t) \tag{13}$$

where $\varepsilon_{in}(t) \leq 0$, $\varepsilon_{re}(t) \geq 0$ and $\varepsilon_{tra}(t) \leq 0$ are the respective strain histories of the transported incident, reflected and transmitted waves. The corresponding displacements read [see Fig. 11(b)]

$$u_{\text{in}}(t) = \int_0^t v_{\text{in}}(t) \mathrm{d}t \tag{14}$$

$$u_{\text{out}}(t) = \int_0^t v_{\text{out}}(t) \mathrm{d}t \tag{15}$$

with the effective displacement $u(t)$

$$u(t) = u_{\text{out}}(t) - u_{\text{in}}(t) \tag{16}$$

It is noted that the measurement of the incoming force F_{in} is less accurate than that of the outgoing force F_{out} at the transmitter bar/specimen interface. Therefore, if the comparison of the incoming and outgoing force histories indicates that the specimen is in quasi-static equilibrium, we evaluate the stress history based on the more accurate transmitter bar measurement, i.e.

$$F(t) = F_{\text{out}}(t) \tag{17}$$

While the measurement accuracy is reduced when calculating the incoming force, it is generally maintained when evaluating the incoming velocities v_{in} from adding the magnitudes of the incident and reflected waves.

Finite Element Model of the Dynamic Experiment

In the dynamic case, a simple two-dimensional model is used to study the mechanical behavior of the split Hopkinson bar device along with the specimen (Fig. 11). The model is used to verify the equilibrium of the specimen, but it is not intended to investigate the response of the experimental set-up in great numerical detail. Instead of using a three-dimensional model, the bars are modeled using plane stress elements (ABAQUS element CPS4R). The round bars are represented by bars of rectangular cross-section. Away from the bar ends, the bars are meshed with elements of an aspect ratio of 1:5 [Fig. 11(a)]. Further, the mesh for the linear elastic bars (E=74 *GPa*, υ=0.3, ρ= 2.82 g/cm^3) is refined within the vicinity of the specimen/bar contact surfaces. A penalty contact algorithm with a friction coefficient of 0.1 is employed to model the interaction between the specimen and bar ends [see encircled regions in Fig. 11(b)].

The specimen is modeled using plane strain elements (Abaqus element CPE4R) along with the same strain-rate independent J2-plasticity model as for the static simulations. Instead of directly modeling the spacer block and the base frame, we impose the boundary condition u_x=0 for the contacting nodes [see encircled nodes labeled 'spacer block' and 'base frame' in Fig. 11(b)]. The same kinematic constraint is applied to all nodes positioned on the symmetry axis of the specimen and the bars. Fracture is taken into account in the dynamic simulations by deleting the elements from the computational model as the equivalent plastic strain exceeds a critical value of 0.3. It is emphasized that no attempt is made to model the real material behavior (which may require the modeling of strain rate and temperature dependency).

Experiments at Strain Rates of 1,075/s

A dynamic experiment is performed on a 28.3 mm wide M-specimen at a striker impact velocity of 4.27 m/s. Figure 12

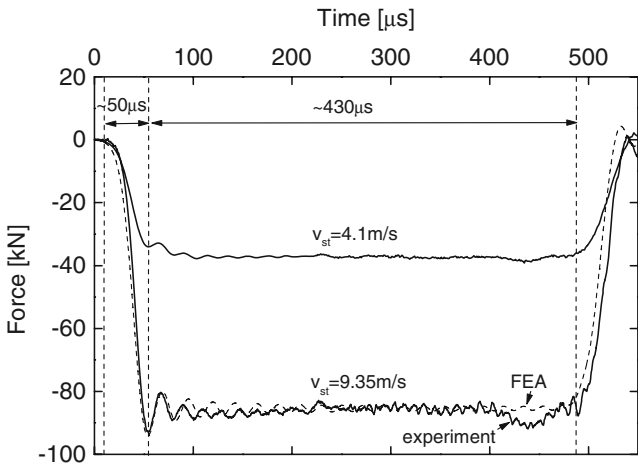

Fig. 10 Characteristic incident waves for distinct striker impact velocities (measurement near the center of the incident bar). The dashed curve labeled "FEA" has been obtained from finite element simulations at the high impact velocity (10 kHz cut-off frequency)

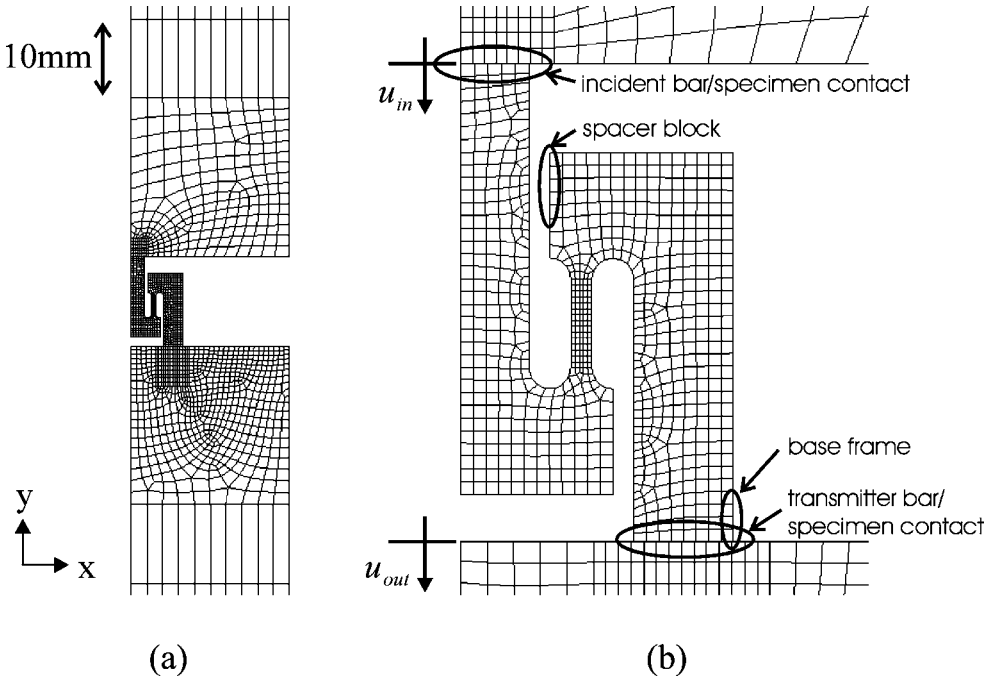

Fig. 11 Two-dimensional FE-model for transient analysis. The meshes of the incident and transmitter bars continue with the same element size (10× 2 mm) along the positive and negative *y*-direction, respectively. The *x*-displacement is set to zero for all nodes of the specimen in contact with the spacer block and the base frame

shows the experimentally-determined time histories of the forces at the specimen boundaries. Both curves are reasonably close which indicates that the hypothesis of quasi-static equilibrium holds true for this experiment (note that the small differences are due to measurement difficulties which will be discussed below). The strain history is shown in Fig. 13(a). The slope of this curve indicates an average equivalent plastic strain rate of about 1,075/s. The stress–strain curve found upon evaluation of equations (3)–(8) is shown in Fig. 13(b). The same graph also shows the resulting stress–strain curve for an experiment performed at 4.11 m/s (open square dots). The matching of the two curves demonstrates the repeatability of this experiment including specimen preparation and the experimental set-up. The comparison of the stress–strain curves for 1,075/s with the static results [dashed line in Fig. 13(b)] indicates that the tested Al2024-351 remains strain rate insensitive within this range of velocities.

Experiments at Strain Rates of 4250/s

Another series of experiments is performed at a striker impact velocity of ν_{st}=9.35 *m/s*. Unlike for the experiments at lower striker velocities, the hypothesis of quasi-static equilibrium can no longer be validated based on the measurement of the incoming and outgoing forces [Fig. 14(a)]. The measurement of the incoming force is not sufficiently accurate since the magnitude of the incident wave (about 90 kN, see Fig. 10) is much larger than the deformation resistance of the specimen (here less than 18 kN). Consequently, both the reflected and incident waves are of the same order of magnitude [Fig. 14(b)]; it is difficult to obtain an accurate estimate of the difference between these two curves (which is proportional to the incoming force) because of a large relative measurement error. Note that the incoming force is small as compared to the magnitude of the reflected and incident wave while the absolute error in the incoming force is large (it corresponds to the sum of the errors in the incident and reflected wave measurements). Therefore, instead of comparing the measured incoming and transmitted force histories, we make use of the computational model to verify equilibrium for the present loading velocity.

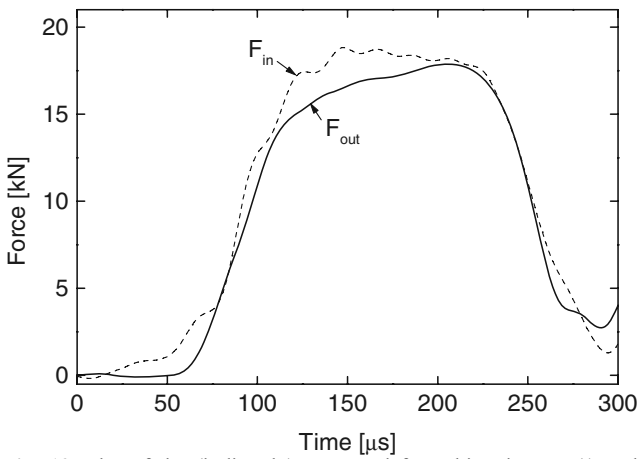

Fig. 12 Plot of the (indirectly) measured force histories F_{in} (*t*) and F_{out} (*t*) at the top and bottom specimen boundaries during an experiment at an equivalent plastic strain rate of about $\dot{\bar{\varepsilon}}^{p} = 1,075/\mathrm{s}$

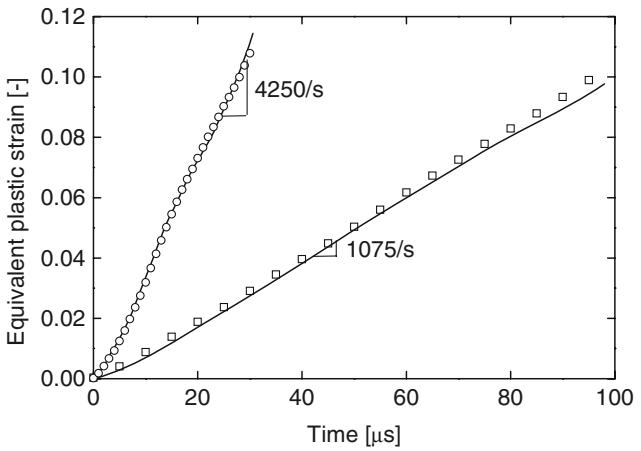

(a)

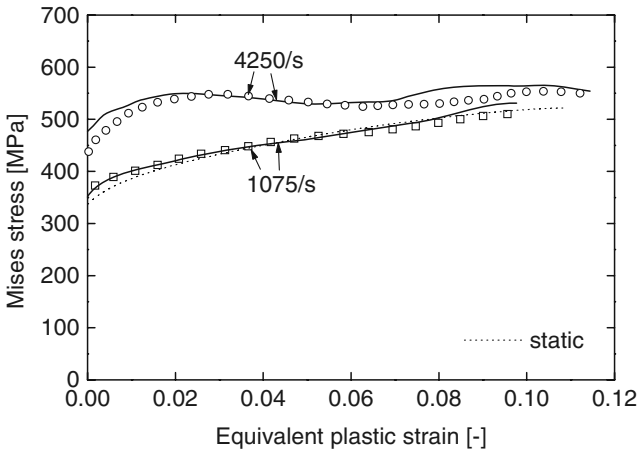

(b)

Fig. 13 Summary of the experimental results: (**a**) Strain history throughout testing, (**b**) stress–strain curves for different equivalent plastic strain rates. Two curves (*solid* and *dotted*) are shown for each strain rate to demonstrate the repeatability of the experiment

Unlike in physical experiments, the contact forces at the specimen/bar interfaces are known in the finite element simulations. Therefore, the response of the simplified numerical model is analyzed for a striker velocity of 9.35 m/s (see dashed line in Fig. 10 for the corresponding incident wave). The computed unfiltered time histories of the contact force at the specimen/incident bar interface ($F_{\text{in}}^{(c)}$) and that at the specimen/transmitter bar interface ($F_{\text{out}}^{(c)}$) are plotted as dashed and solid curves in Fig. 14(c). The comparison of these two curves shows that the specimen is still in quasi-static equilibrium (the maximum difference in the mean force level is about 3%).

Contrary to the incoming force measurement, the accuracy of the incoming velocity/displacement measurement [see equation (12)] is not reduced by the mismatch of the incident force and the specimen resistance. Analogously to the evaluation of the previous experiments, the equivalent plastic strain history is determined from equations (3)–(8). The results indicate an average plastic strain rate of about 4,250/s [Fig. 13(a)]. The corresponding Mises stress versus equivalent plastic strain curve is depicted in Fig. 13(b). Again, we observe reasonable repeatability of the experiment at 4,250/s. It is noted that the deformation resistance of Al2024-T351 increases substantially when increasing the average strain rate from 1,075 to 4,250/s.

Discussion

The proposed experimental technique has been validated for strain rates of up to 4,250/s. The performance at higher strain rates is not investigated. However, it may be expected that reliable results can still be obtained for much higher strain rates. In the present experiments, the entire specimen has been in quasi-static equilibrium. When testing at even higher velocities, one may relax this constraint and apply the requirement of quasi-static equilibrium to the path D-C-B-A only [Fig. 2(a)]. In other words, there may still be a significant potential in increasing the loading velocity while maintaining quasi-static equilibrium.

The issue of determining the displacement to fracture under dynamic loading conditions needs to be addressed in future research. Advanced optical techniques [10] cannot be applied in the present case since fracture initiates away from the visible specimen surface. Alternatively, the displacement to fracture may be determined from the force–displacement curve. The sudden drop of the force level due to fracture may be considered as a very high frequency pulse which is introduced into the transmitter bar. The challenge is to measure the full frequency content of this force history at the specimen-bar interface using the strain gage positioned at a distance of several bar diameters away from the bar end. It appears that the conversion of a local load applied at the end of the bar (note that the specimen contact area is significantly smaller than that of the bar) into an approximately one-dimensional wave (which is recorded by the strain gage) involves some physical filtering of high frequencies, i.e. despite of the high bandwidth of the strain gage measurement, some information is “lost” (from the classical one-dimensional perspective) due to three-dimensional effects at the end of the bar. The simulation results in Fig. 14(d) illustrate this loss of information in a qualitative manner. The dashed line depicts the outgoing force as determined from the strain at the position of the transmitter bar strain gage, while the solid line corresponds to the direct output of the contact force at the transmitter bar/specimen interface. Both measurements are essentially equivalent prior to fracture. However, as fracture initiates, the contact force drops abruptly while the strain gage recording shows a much smoother decrease of the force level. Unless theoretical

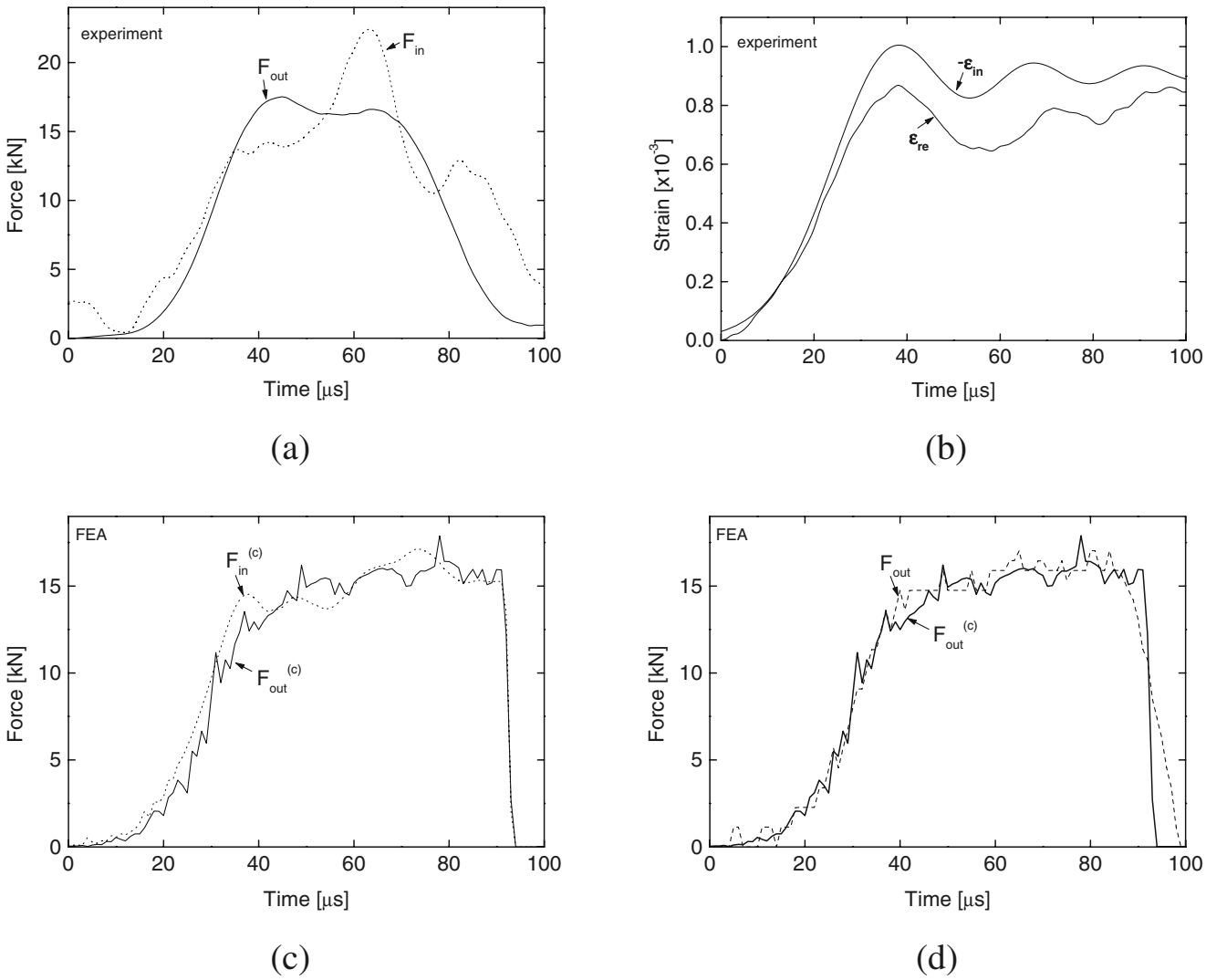

Fig. 14 Verification of the equilibrium and force measurement for dynamic testing at 9.2 m/s: (**a**) Experimentally-determined forces at the specimen boundaries (indirect measurement), (**b**) measured incident and reflected wave after dispersion-corrected shifting to the incident bar/specimen interface (direct measurement of the strain in the incident bar), (**c**) contact forces at the specimen/bar interface as obtained from finite element analysis, (**d**) comparison of the contact force at the specimen/transmitter bar interface (*solid curve*) with the outgoing force computed from the transmitted strain wave (*dashed line*)

solutions are found, reliable three-dimensional finite element models (significantly more advanced and efficient than the simple model used in the present study) need to be developed and validated experimentally in order to solve the inverse problem of determining abrupt changes in the force level at the end of the bars based on conventional strain gage measurements.

The present technique is limited in its applicability to materials for which some features of the constitutive response are known a priori. Here, we make use of the Levy–von Mises material model to derive the uniaxial stress–strain within the gage section from global measurements. However, it is noted that the same concern applies when a three-dimensional Levy–von Mises material model is calibrated based on uniaxial tensile tests.

Conclusion

Experimental issues related to the gripping of tensile specimens are successfully eliminated using the proposed technique. It consists of an M-shaped specimen which is subject to high velocity impact loading. Inside the specimen, the incoming pressure pulse is converted into tensile loading of the specimen gage section. Consequently, the specimen can be used in a conventional split Hopkinson pressure bar without the need of additional grips or special attachments. The M-specimen gage section is designed for transverse plane strain. The transverse plane strain concept is of particular advantage in dynamics since it retards necking and allows for very short gage sections. This new experimental technique has been validated for dynamic

tensile testing at strain rates of up to 4,250/s. The experimental results demonstrate that the measured force–displacement curves are still free from severe oscillations at these high strain rates.

Acknowledgement The authors are grateful to Mr. R. Barre and Mr. R. Herbez for their technical assistance in performing the dynamic experiments. Thanks are due to Professor T. Wierzbicki and Mr. C. Walters from MIT for valuable discussions. Altair Engineering is thanked for providing the pre-processing software Hypermesh.

References

1. Hopkinson B (1914) A method of measuring the pressure produced in the detonation of high explosives or by the impact of bullets. Philos Trans R Soc Lond, A 213:437–456.
2. Kolsky H (1949) An investigation of mechanical properties of materials at very high rates of loading. Proc Phys Soc, B 62:676–700.
3. Duffy J, Campbell JD, Hawley RH (1971) On the use of a torsional split Hopkinson bar to study rate effects in 1100-0 aluminium. J Appl Mech 38:83–91.
4. Harding J, Wood EO, Campbell JD (1960) Tensile testing of materials at impact rates of strain. J Mech Eng Sci 2(2): 88–96.
5. Nicholas T (1981) Tensile testing of materials at high rates of strain. Exp Mech 21(5):177–185.
6. Luong MP (1990) Tensile and shear strength of concrete and rock. Eng Fract Mech 35(1–3):127–135.
7. McClintock FA, Zheng ZM (1993) Ductile fracture in sheets under transverse strain gradients. Int J Fract 64(4):321–337.
8. Gary G (2005) DAVID Instruction manual, Palaiseau, France, http://www.lms.polytechnique.fr/dynamique/greef/web4034_david.html.
9. Zhao H, Gary G (1996) On the use of SHPB technique to determine the dynamic behaviour of the materials in the range of small strains. Int J Solids Struct 33:3363–3375.
10. Verleysen P, Degrieck J (2004) Optical measurement of the specimen deformation a high strain rate. Exp Mech 44(3):247–252.